Short-range order in solid and liquid KBr probed by EXAFS

Short-range order in solid and liquid KBr probed by EXAFS

Andrea Di Cicco†, Mauricio Jose Rosolen†¶, Roberto Marassi‡, Roberto Tossici‡, Adriano Filipponi§ and Jaroslaw Rybicki‖

† UdR INFM, Dipartimento di Matematica e Fisica, Università degli Studi di Camerino, Via Madonna delle Carceri, 62032 Camerino (MC), Italy
‡ Dipartimento di Chimica, Università degli Studi di Camerino, Via S Agostino, 62032 Camerino (MC), Italy
§ ESRF, BP 220, 38043 Grenoble, France
‖ Faculty of Technical Physics and Applied Mathematics, Technical University of Gdansk, Naturowicza 11/12, 80-952 Gdansk, Poland

Abstract. Br K-edge EXAFS spectra of solid and liquid KBr have been performed and analysed using advanced techniques for data analysis (GNXAS). Structural results on solid KBr at room temperature and near melting are compared with molecular dynamics (MD) simulations and diffraction data. The first-neighbour distribution is found to be strongly asymmetric even at room temperature, as also shown by MD simulations. This confirms the existence of important anharmonic effects in solid KBr. MD simulations are in agreement with EXAFS data at room temperature. For solid KBr near melting, anharmonic effects become very important. In comparison with MD calculations, the rise of the first-neighbour peak is found to be steeper, while the foot of the first-neighbour distribution is found to be slightly shifted toward longer distances. Experimental short-range partial pair distribution functions g_{BrK} and g_{BrBr} are derived in liquid KBr for the first time. The first peak of the g_{BrK} distribution is accurately determined and found to be in good agreement with MD simulations, confirming a slight contraction of the most probable Br–K distance in the liquid phase. The first peak of the g_{BrBr} distribution, measured with less accuracy, is found to be sharper and slightly shifted to longer distances, lowering the overlap with the first-neighbour K shell.

1. Introduction

Solid and molten alkali halides are an important class of binary systems which have been studied for a long time due to their peculiar physical and chemical properties. They are considered as the prototype of the ionic insulators and have been largely used by scientists as test systems both in crystalline and solid phases, due to their intrinsic simplicity.

Reliable expressions for the interatomic potential have been developed and used to investigate microscopic properties of molten alkali halides, mainly through computer simulations [1–3]. Local structure in solid and liquid alkali halides was studied since the earlier times using Monte Carlo (MC) simulations [4–7]. Molecular dynamics (MD)

¶ Permanent address: Universidade de Sao Paulo, Insituto de Quimica de Sao Carlos-IQSC, Av. Dr Carlos Botelho, 1465 Sao Carlos-SP-Brazil 13560-970.

calculations have been widely used to study the structure and dynamics of almost all molten alkali halides [2,8–14].

The current knowledge of atomic structure and dynamics of solid and liquid alkali halides is based mainly on experimental results obtained by accurate elastic and inelastic diffraction experiments. However, detailed studies were carried out only on a few liquid and high-temperature solid systems. The local structure of liquid alkali chlorides was investigated using neutron diffraction (ND) and the isotopic substitution technique, taking advantage of the different scattering lengths of the Cl isotopes (see [15–17] and the reference list in [1]). In those systems, good agreement between partial pair distribution functions derived by diffraction measurements and theoretical simulations was usually achieved. However, few ND measurements using the isotope substitution technique are actually available. In fact, there are practical difficulties in the use of suitable isotopes or mixture of isotopes. Moreover, signal-to-noise ratios and Q extension of some $S(Q)$ measurements are sometimes unsatisfactory.

In this context, the x-ray absorption spectroscopy (XAS) can play an important role. In fact, the extended x-ray absorption fine structure (EXAFS) signal is extremely sensitive to the short-range structure around selected atomic sites both in solid and liquid phases [18]. Low-noise EXAFS spectra of high-temperature solid and liquid systems can be easily recorded at any atomic core-level edge, excluding only low-Z elements [19]. These measurements can complement those obtained by diffraction techniques. In fact, recently developed advanced data-analysis methods [20, 21] using *ab initio* multiple-scattering (MS) calculations have been shown to give reliable information on the local structure of simple monatomic liquid and amorphous systems [22–26].

In this paper, we present a detailed study of the low-noise Br K-edge EXAFS spectra of solid and liquid KBr using those advanced data-analysis techniques (GNXAS) and molecular dynamics (MD) simulations. KBr is a good example of an alkali halide system and represents a strict test of the reliability and accuracy of present theoretical models. Structural and dynamical properties of low-temperature solid KBr have been widely studied using several experimental and theoretical methods. Important deviations from the harmonic approximation have been observed in solid KBr [27, 28] even at relatively low temperatures. Previous EXAFS studies have also pointed out the importance of anharmonic contributions in alkali halides [29, 30].

Comparison of short-range pair distribution functions derived by EXAFS and results of MD simulations in the same thermodynamic conditions allow us to derive new and accurate information about deviations from the harmonic model in solid KBr. In particular, the first-neighbour distribution in solid KBr at room temperature and near melting, never measured before, can be accurately reconstructed from EXAFS data.

Application of EXAFS is particularly interesting for liquid KBr. In fact, in this case the isotope substitution technique is difficult to apply and no neutron diffraction measurements are available. Our EXAFS measurement of liquid KBr provides the possibility for the first structural study of this liquid system and a direct comparison with the short-range partial pair distribution functions g_{BrK} and g_{BrBr} obtained by MD simulations.

The paper is organized as follows: in section 2 a description of the experimental details concerning preparation of samples and x-ray absorption measurements is reported; in section 3 we describe MD calculations in solid and liquid phases; section 4 contains results and a discussion on EXAFS data-analysis of solid and liquid KBr; section 5 is devoted to the conclusions.

2. Experimental

X-ray absorption measurements near the Br K-edge were performed in transmission mode at LURE (Laboratoire pour L'Utilisation du Rayonnement Electromagnètique) on the EXAFS I (D-42) and EXAFS IV (D-44) beam-lines (DCI storage ring) equipped with a channel-cut Si (331) and a double crystal Si (311) monochromators respectively. The DCI ring was operating at 1.85 GeV with a typical current of 300 mA. The typical energy resolution obtained in these measurements is about 3 eV HWHM (half width half maximum) at the Br K-edge threshold energy.

Suitable samples of KBr were prepared and tested in advance, taking care of the severe requirements of thickness and homogeneity needed to perform accurate XAS measurements, especially in the liquid phase. Particular care was also taken to avoid water contamination. Finely ground powders of KBr, 99.9+% purity (Aldrich), were dispersed in water-free ethanol under stirring using an ultrasonic bath.

The suspension was left at rest for some time to allow precipitation of the largest particles. Average particle size was in the μm range. The same procedure was followed to prepare suspensions of boron nitride (BN). The suspensions were decanted and mixed together in such a way to obtain appropriate BN-to-KBr weight ratios. The initial weight proportion was about ten to one for the sample designed for liquid phase measurements and about twice as big for solid phase samples.

The final suspensions were then filtered using Millipore polycarbonate membranes under an inert gas atmosphere. This procedure permits to obtain a random dispersion of particles of KBr powders into the BN matrix. The mixed powders were dried and pressed at about 7 kbar in an argon filled dry-box (moisture content typically lower than 5 ppm). This original preparation technique was proved to be successful for high-quality measurements at high temperatures [19]. The final samples were pellets of about 1 cm diameter with thickness of the order of 1 mm, stored under vacuum into glass tubes. Thicknesses of the samples were chosen in order to obtain the best signal-to-noise ratio in absorption measurements. Optimization of samples was performed at the University of Camerino using XAS laboratory equipment.

High-temperature measurements were performed by using a specially designed furnace [19]. In this experiment, the pressure inside the furnace was around 10^{-5} bar at the highest temperatures measured by a chromel–alumel thermocouple. Before any measurements were taken, each sample was heated in vacuum above 200°C for about 30 minutes to remove any residual moisture from the sample and the crucible.

Typical x-ray absorption near-edge structure (XANES) as a function of temperature are reported in figure 1, where absorption spectra of solid KBr at 520, 700, 870 and 940 K (solid lines) are directly compared with the signal of liquid KBr at 1025 K (crosses). Absorption spectra of the solid phase as functions of temperature show a continuous broadening of the XANES features, while the liquid phase spectrum shows a drastic change.

The KBr sample starts to evaporate upon melting ($T_m = 1007$ K), therefore a decrease of the absorption coefficient, due to a decreased effective thickness, was observed as a function of time. For this reason, samples for liquid phase measurements were chosen to have higher absorption jumps (initial $\Delta\alpha \sim 2$) with respect to that used for solid phase measurements ($\Delta\alpha \sim 0.8$). The absorption coefficient $\alpha_j(E)$ of the jth scan was found to follow quite closely an exponential decay model for each energy point E_i:

$$\alpha_j(E_i) = \alpha_{(0)}(E_i) \exp\left[-\frac{(t_0 + i\,\Delta t + jN\,\Delta t)}{\tau}\right] \tag{1}$$
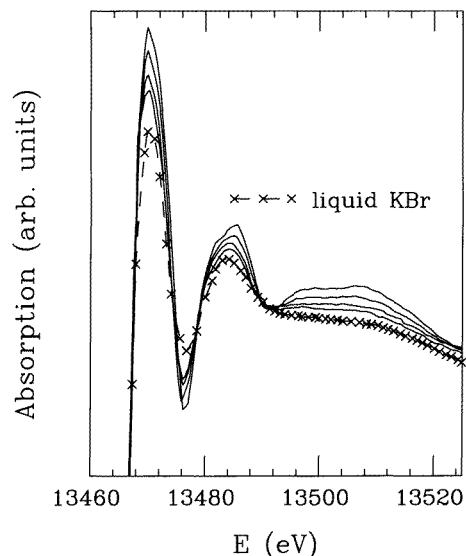
Figure 1. Br *K*-edge XANES spectra of solid KBr at 520, 700, 870 and 940 K (solid curves) compared with the XANES spectrum of liquid KBr at 1025 K (crosses, dashed).

where t is the time, Δt is the measuring time for each energy point, t_0 is the initial time of the measurement (considered equal to zero), N is the total number of energy points, and τ is the characteristic decay time. $\alpha_{(0)}$ is the ideal absorption coefficient in the case of constant effective thickness.

Equation (1) corresponds to a simple model for evaporation:

$$\mathrm{d}\rho_A/\mathrm{d}t = -\rho_A/\tau \tag{2}$$

where the rate of evaporation is proportional to the density of photoabsorbing atoms ρ_A contained in the sampled volume.

The performance of several successive scans of the absorption coefficient allowed us to use a least-squares fitting routine from which a robust estimate of τ and a reconstruction of the ideal absorption coefficient at the time t_0 can be obtained. The procedure is quite reliable because all of the post-edge energy points can be used. In our case the decay time turned out to be $\tau \sim 3500$ s and the uncertainty in the amplitude in the reconstructed $\alpha_{(0)}$ is estimated to be below 5%. A slightly better fit of the decaying trend is obtained adding a constant term to (1), i.e. considering a non-zero limiting value for the asymptotic thickness. However, the reconstructed $\alpha_{(0)}$ spectra obtained using both approaches coincide within the error. The final spectrum used for liquid phase measurements was reconstructed using five successive scans.

The EXAFS spectra were recorded in a quite extended energy range (13300–14500 eV at room temperature and 13300–14000 eV at high temperature), using a constant wave vector scale above the edge ($\Delta k = 0.04$ Å^{-1}) with a minimum energy step of 0.5 eV. The total number of experimental energy points was 433 for the room temperature spectrum and 320 for the high temperature ones. The total integration time was about 6 s (solid phase spectra) and 10 s (liquid phase measurements) per energy point with about 50 kcounts/s and 250 kcounts/s on the ionization chambers I_0 and I_1 respectively. The resulting statistical noise was found to be $\sigma \sim 2 \times 10^{-4}$ (standard deviation).

3. A model for local structure: molecular dynamics simulations

Microscopic properties of alkali halides, especially in their liquid phase, have been extensively investigated in the last 25 years using various simulation techniques (see for example [1, 7] for reviews). Reliable pair interatomic potentials were developed a long time ago and general agreement with available experimental data was found. In particular, Monte Carlo [4–7] and molecular dynamics [2,8,10–14] simulations have been used to study almost all of the molten alkali halides.

In this paper we compare for the first time experimental and theoretical results on short-range structural properties of liquid and solid KBr. In fact, EXAFS is able to probe the short-range $g(r)$ in solid and liquid systems with high accuracy and a deep insight into the atomic interaction potential can be gained by comparison with reliable computer simulations.

Molecular dynamics (MD) simulations were performed using the classic Tosi–Fumi two-body interaction potential [31] for a system containing 500 KBr molecules. In the solid state the simulations were realized in the isobaric–isoenthalpic (NpH), and isobaric–isothermal (NpT) [32] ensembles, giving similar results, whereas in the liquid state the microcanonical (NVE) ensemble was used. The MD results for solid KBr quoted in the present work are taken from the NpH runs.

A crystalline structure was prepared at 300 K by assigning to the ions their initial velocities from the Maxwell distribution, then equilibrated during 5.0×10^{-11} s (20 000 time steps), and sampled over another 5.0×10^{-11} s. The resulting structure was submitted to a stepwise heating up to 1150 K (with temperature step of 150 K up to 900 K, and of 50 K for higher temperatures). At each intermediate temperature the system was thermalized and sampled during the same time intervals used at 300 K. The average temperatures of the two simulations presented in this work were 303 K and 948 K (nominal temperatures are 300 K and 950 K respectively).

At the temperature of 1150 K obtained as described above the system remained crystalline, showing, however, high temperature fluctuations, and a remarkable widening of radial distribution peaks. Melting was realized by using various ensembles, as well as different heating and temperature scaling schemes, always obtaining analogous equilibrium liquid structures. The results obtained are of course related to the particular shape of the interaction potential that has been used (the Tosi–Fumi parametrization was originally determined by fitting to the solid state properties). In particular, the liquid structure considered below was obtained in the following way: the temperature of 1200 K was applied, and after about 1.0×10^{-11} s the lattice destabilization occurred, accompanied by the onset of linear increase of ions mean square displacements versus time. The resulting configuration was then equilibrated in the microcanonical ensemble over 20 000 time steps, and sampled over 50 000 time steps (total energy fluctuations less than 0.01%). During the thermalization the temperature decreased to about 1100 K, and the average temperature during the sampling was 1093 K.

In figure 2(a), the total Br–all pair distribution $g(r)$ in solid KBr at 300 K, 950 K and liquid KBr at 1100 K are shown ($\diamond$). Peaks of the distribution function in solid KBr are due to the shells of neighbours and their widths are related to the amplitude of the vibrational modes. Important anharmonic effects, leading to non-Gaussian shapes of the individual shell distributions, are known to be present even at very low temperatures in alkali halides and in particular on KBr. Evidence for these effects has been found, for example, in x-ray [27] and neutron [28] diffraction and previous EXAFS [29] studies.

A very good fit of the pair distribution function is performed using suitable analytical expression for each individual shell. The clear asymmetry of the first-neighbour peak at
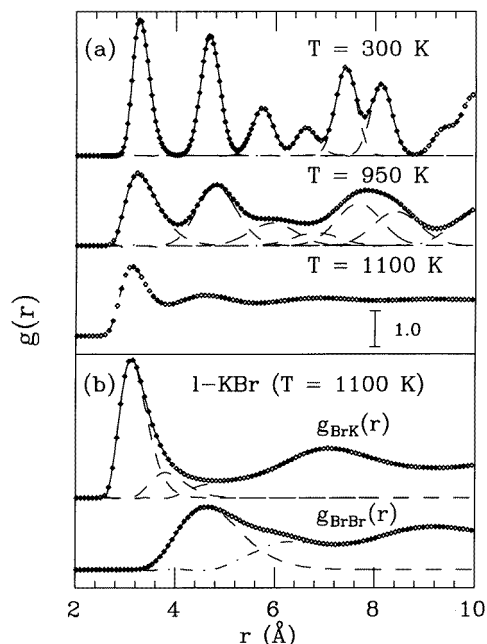
Figure 2. Upper panel (a): total (Br–all) pair distribution functions of solid (300 K, 950 K) and liquid KBr (1100 K) as calculated from MD simulations ($\diamond$). Dashed curves are the individual best-fit shell distribution modelled as Γ or Gaussian functions. Solid lines are the total best-fit distribution functions and dot-dashed lines are the residuals. Lower panel (b): partial g_{BrK} and g_{BrBr} distribution functions for liquid KBr. Dashed curves are the best-fit Γ functions describing the short-range peaks of the pair distributions. Long-range tails (residuals) are shown dot-dashed.

300 K and 950 K, can be accounted for using a Γ-like function for the first-neighbour bond length probability density. The general expression [25] for a peak of the pair distribution function associated with the jth shell of neighbours is:

$$g_j(r) = \frac{N}{4\pi\rho r^2} \frac{2}{\sigma|\beta|\Gamma(\frac{4}{\beta^2})} \left(\frac{4}{\beta^2} + \frac{2(r-R)}{\sigma\beta}\right)^{\frac{4}{\beta^2}-1} \exp\left[-\left(\frac{4}{\beta^2} + \frac{2(r-R)}{\sigma\beta}\right)\right]. \tag{3}$$

Equation (3) is defined for $(r-R)\beta > -2\sigma$ and depends on four parameters N, R, σ^2, β: for the jth shell these are respectively the coordination number N_j, the average distance R_j, the variance σ_j^2, and the dimensionless skewness parameter $\beta_j = K_3^j/\sigma_j^3$, where K_3^j is the third cumulant of the distribution. $\Gamma(p)$ is the Euler gamma function and is calculated for $p = 4/\beta_j^2$ defined on the positive real axis. In the crystalline case the coordination numbers N_j have been kept fixed to the known crystallographic values. ρ is the actual density of the calculation. The shape of the Γ-like function can be varied from positive to negative asymmetry through the Gaussian limit $\beta_j = 0$. The distribution of (3) can accurately model the actual peak shape obtained by MD simulations and has the important advantage of having only one parameter related to the higher-order cumulants, thus reducing the number of floating variables.

In table 1 we report the best-fit parameters obtained for each individual neighbour shell for MD calculations at $T = 300$ K and $T = 950$ K. Distance variances σ^2 and skewness

Table 1. Structural parameters related to the first four neighbour shells in solid KBr derived from MD simulations at room temperature and near the melting point ($T_m = 1007$ K). Coordination numbers (deg), average distance R, variance σ^2 and skewness β (dimensionless) are specified for each shell. The lower part of the table contains cell size a and mean square vibrational amplitudes derived from neutron (ND) and x-ray (XRD) diffraction experiments.

Shell (deg)	Parameters	$T = 300$ K	$T = 950$ K
Molecular dynamics (this work)			
I (6)	R_1 (Å)	3.324	3.494
	σ_1^2 (10^{-3}Å^2)	30.4	161
	β_1	0.464	0.924
II (12)	R_2 (Å)	4.695	4.90
	σ_2^2 (10^{-3}Å^2)	36.2	163
	β_2	0.086	0.186
III (8)	R_3 (Å)	5.746	5.99
	σ_3^2 (10^{-3}Å^2)	44.5	202
IV (6)	R_4 (Å)	6.62	6.86
	σ_4^2 (10^{-3}Å^2)	42	225
Experimental technique			
XRD [33]	a (Å) ($T = 298$ K)	6.5982(2)	
XRD [33]	a (Å) ($T = 350$ K)	6.6060(5)	
[27][a]	a (Å) ($T = 1000$ K)		6.76
XRD [27]	$\langle u^2 \rangle_{mean}$ (10^{-3}Å^2)	30	140
ND [28]	$\langle u_{Br}^2 \rangle$ (10^{-3}Å^2)	32.3(9)	
($T = 295$ K)	$\langle u_K^2 \rangle$ (10^{-3}Å^2)	27.9(5)	

[a] Extrapolation of thermal expansion results.

Table 2. Structural parameters related to the first peak of the partial $g_{BrK}(r)$ and $g_{BrBr}(r)$ distribution functions in l-KBr as determined from MD simulations. Average distance R, σ^2, skewness β (dimensionless) and coordination number N are specified for each Γ function (Peak).

Peak	N	R (Å)	σ^2 (10^{-3}Å^2)	β
g_{BrK}				
I	3.64	3.266	92.5	0.707
II	1.27	3.988	148	0.627
g_{BrBr}				
I	8.79	4.995	490	0.579

β increase as a function of temperature. The asymmetry is more evident for the first-neighbour distribution, while is very weak for farther shells. The third and fourth shells can be considered essentially Gaussian ($\beta = 0$). In the lower part of table 1 we reported the cell parameter a (KBr has cubic symmetry) as measured by x-ray diffraction. The currently accepted value at room temperature is 6.5982 (2) Å, although deviations (up to 0.02 Å) from this value have been reported in different studies [33]. The R_4 (Br–Br) value (6.62 Å) obtained by MD simulation is in good agreement with diffraction. In the comparison, it should be also considered that (i) the average R_4 value could be slightly longer than the measured a value, because of the positive contribution of vibrations perpendicular to the Br–Br direction and (ii) the temperature of the simulation could correspond to a slightly different effective temperature. Moreover, an additional complication arises when the distribution is

not symmetric ($\beta > 0$), because the distance value R is shifted toward longer distances and no longer corresponds to the maximum of the distance distribution. MD calculations give reasonable values also for vibrational amplitudes. In fact, the mean square vibrational amplitudes $\langle u^2 \rangle$ measured by diffraction represent limiting values for distance variances σ^2. For a couple of atoms A and B, the uncorrelated limit is $\sigma^2 = \langle u_A^2 \rangle + \langle u_B^2 \rangle$. The first-neighbour bond variance obtained by MD simulations is about one half the limiting value $\langle u_{Br}^2 \rangle + \langle u_K^2 \rangle$, due to the correlation in the motion of neighbouring atoms. The distance variance of farther shells increase without exceeding the uncorrelated limit. From these considerations, we conclude that the model for local structure and dynamics of solid KBr given by the present MD simulation is consistent with previous experimental determinations. In the next sections we compare the short-range pair distribution function of solid KBr obtained by MD simulations with that determined by EXAFS spectroscopy.

In figure 2(b), the partial $g_{BrK}(r)$ and $g_{BrBr}(r)$ distribution functions in liquid KBr obtained by MD simulations at 1100 K are shown ($\diamond$). In this case, there is no clear separation between the shell of neighbours. However, it is still possible to identify short-range peaks merging in continuous long-range oscillatory tails. The decomposition in short-range peaks and long-range tails is particularly important for the successive EXAFS data analyses of liquid KBr. The short-range peaks can again be modelled using Γ functions (dashed curves in figure 2(b)). The first-neighbour peak of the $g_{BrK}(r)$ function has been modelled using two Γ functions in order to follow more closely its strongly asymmetric shape. Parameters of the Γ functions are reported in table 2. Those values are used as starting values for the refinement of local structure of liquid KBr presented in the next sections.

4. Data analysis

4.1. Solid KBr

EXAFS spectra of solid KBr at room temperature and near melting (940 K) were analysed using multiple-scattering calculations in the framework of a recently developed *ab initio* data-analysis method (GNXAS) [20, 21]. This method is based on an n-body expansion of the x-ray absorption cross-section where only the lower-order terms are retained. In the present case, we considered only two-body ($\gamma^{(2)}$) and three-body ($\gamma^{(3)}$) MS contributions, while four-body terms were found to be negligible in the energy range under consideration.

Data analysis was performed taking into account double-electron excitation channels into the atomic background. In fact, at the Br K-edge, sizeable contributions associated with the opening of the [1s3d] and [1s3p] double-electron excitation channels occur at about 90 and 200 eV above the edge respectively. The contribution of double-electron excitation channels in x-ray absorption Br K-edge spectra was studied in gas-phase Br_2, HBr [34] and brominated hydrocarbon molecules [35] as well as in solid and liquid alkali bromides [30,36,37]. We refer to [34, 35] for details on the accurate modelling of the double-electron [1s3d] and [1s3p] channels.

Using the GNXAS method, the structural analysis is performed by minimizing a standard χ^2-like residual function R, i.e. optimizing the agreement between a model absorption $\alpha_{mod}(E)$ and the experimental $\alpha_{exp}(E)$ signals. Using such a procedure, a full statistical evaluation of the structural results can be performed taking into account the noise of the experimental data [21]. In particular, it is possible to calculate the expected value of the residual function R and evaluate the quality of the fit. Moreover, statistical errors on the structural parameters can be estimated according to a specified confidence level [21].

Both background and structural parameters are refined at the same time. The background parameters include the usual polynomial functions and the empirical shapes of the [1s3d] and [1s3p] channels. The structural signal is simulated using multiple-scattering contributions associated with short-range two-atom and three-atom configurations. The structural parameters are those defining those atomic configurations. The MS signals were calculated using the complex Hedin–Lundqvist (HL) potential in the framework of the muffin-tin approximation [20, 38]. Tangent sphere radii were used for phase-shift calculations. Starting parameters for two-atom configurations are those listed in table 1, while three-body configurations involving first-neighbour distances are (degeneracy in brackets): (i) K–Br–K 90° (12); (ii) Br–K–Br 90° (24); (iii) K–Br–K 180° (3); (iv) Br–K–Br 180° (6). All of these triangular configurations are defined by two Br–K first-neighbour distances and the 90 or 180° angle [20, 21]. We have found that the use of the first four two-body and three-body MS signals, associated with the above-mentioned pair and triplet configurations, is sufficient to explain the EXAFS spectrum of solid KBr at 300 K.
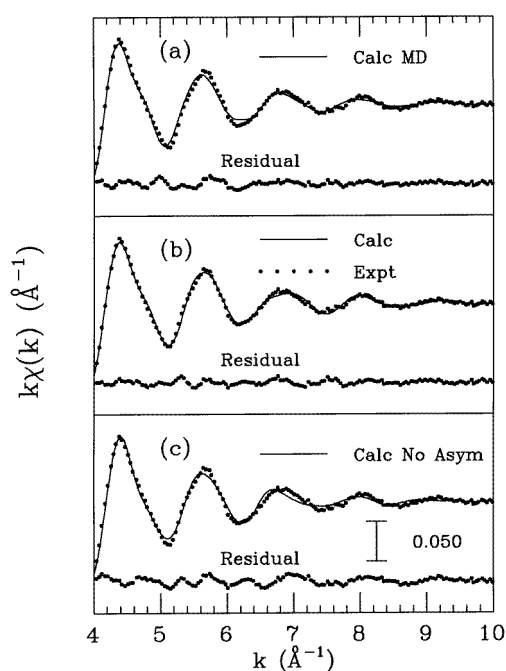
Figure 3. Multiple-scattering calculations (solid lines) compared with the experimental EXAFS $k\chi(k)$ structural signal (dots). In the upper panel (a), we compare the calculation based on the model structure provided by MD simulations (Calc MD) and the experimental EXAFS spectrum. The overall agreement is quite good. The centre panel (b) shows the comparison between the best-fit signal (Calc) obtained by refinement of the local structure and the experimental one. The agreement is very good, as also shown by the residual curve. In the lower panel (c) we show the best-fit curve obtained using simple Gaussian models for the shell distributions. The residual curve shows that anharmonic contribution must be taken into account in the modelling of the Br K-edge experimental spectrum at 300 K. EXAFS spectra are thus found to be very sensitive to the asymmetry of the first-neighbour distribution function.

A first important test can be made by optimizing only background and non-structural parameters while using the average structural parameters derived from MD simulations (see

section 3). In this way, the local structure obtained using MD can be directly compared with experimental data. In figure 3(a), we report the comparison between the experimental EXAFS signal $k\chi(k)$ (dots) of solid KBr at 300 K and that calculated (calc MD) using the model structure, including vibrations, given by MD. The agreement is quite good, confirming the quality of the theoretical models. However, the residual function R is about twice the expected value. In fact, the residual curve (lower curve in (a)) shows clear oscillations, suggesting that refining of local structure is needed.
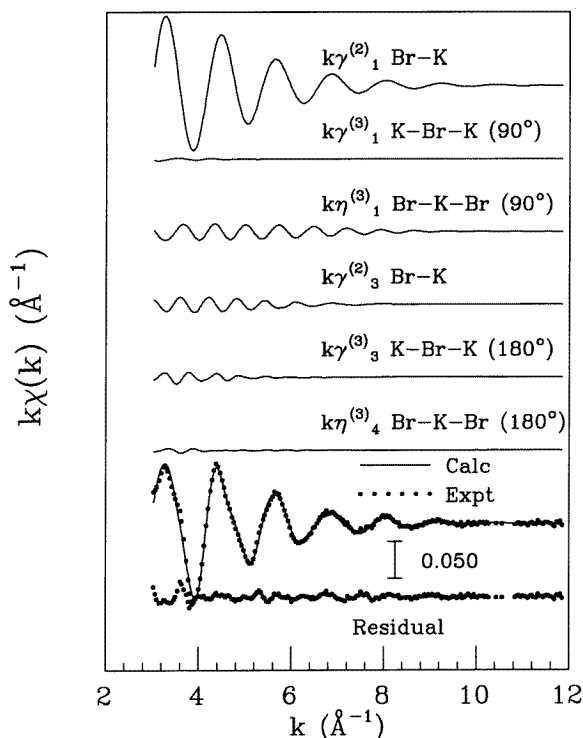
Figure 4. Multiple-scattering (MS) best-fit calculations (solid lines) compared with the experimental EXAFS $k\chi(k)$ structural signal (dots). The dominant two-body $k\gamma_1^{(2)}$ signal associated with the first-neighbour K atoms is the upper curve. The other curves in the middle part of the figure are the MS signals related to the farther shell. The agreement between the sum of the multiple-scattering signals (Calc, solid line) and the experimental spectrum (Expt, dots) is very good, as also shown by the residual curve (dashed).

The dominant contribution to the EXAFS spectrum is the first-neighbour Br–K $\gamma_1^{(2)}$ MS signal. Refinement of the first-neighbour distribution requires only optimization of three parameters R_1, σ_1^2 and β_1. These parameters are the more important ones and can be accurately measured by EXAFS. However, a more complete refinement can be carried out including the variation of the other two-body and three-body signals up to the fourth shell of neighbours. Coordination numbers have been kept fixed to crystallographic values. The second and fourth two-body Br–Br $\gamma^{(2)}$ signals have been grouped with the corresponding Br–K–Br $\gamma^{(3)}$ ones, using effective $\eta^{(3)}$ signals which depend on the same structural parameters (see [20, 21]). Average angle values have been kept fixed. A Gaussian distribution (described by variance σ^2) has been used for the third shell two-body $\gamma_3^{(2)}$ Br–K

signal. Thermal damping of three-body signals is performed using covariance matrices [20, 21]. In the present case, a number of 10 parameters is required: the variances ($\sigma_\theta^{(2)}$) of the four angular distributions; the bond–bond correlations ($\rho_{r,r'}$); the two bond–angle correlations for the 90° configurations [21]. Detailed discussion on the configurational average of three-body signals related to isosceles (90°) and collinear (180°) configurations are reported elsewhere [20, 21]. Fitting of solid KBr at 300 K was then performed using a total number of 16 parameters, including the non-structural E_0 (accounting for the difference between the experimental and theoretical energy scales) and S_0^2 (many-body and normalization correction) ones.

In figure 4 the various MS components of the simulated best-fit EXAFS signal (calc) are shown and compared with the experimental signal. As anticipated, the dominant signal is the Br–K two-body one, although some signals related to farther shells are not negligible. The agreement between calculated and experimental signal is very good. The R function is only 1.2 times the expected value and the residual curve is almost flat (see also figure 3(b)).

Mean distances and variances of farther shells can be easily calculated from the three-body parameters used in the minimization procedure [21]. In table 3 we report values of the best-fit structural parameters obtained by EXAFS experimental data, which can be directly compared with those derived from MD simulations reported in table 1. Statistical errors on structural parameters have been evaluated accounting for correlations among parameters and are indicated in brackets [21] The amplitude reduction factor was found to be $S_0^2 = 0.80$ (5) at all temperatures under consideration. The E_0 energy was found to be about 5 eV above the inflection point, as expected in this ionic compound.

Previous EXAFS studies [29, 30] reported investigations of solid alkali halides at high pressure and/or at low temperature. Both studies pointed out the importance of taking account of the third cumulant of the first-neighbour distribution (related to the parameter β measured in the present work). Absolute values of first-neighbour average distance and variance at ambient pressure and temperature reported in these works [29] differ from literature values and present results obtained by EXAFS and MD simulations although the skewness parameter β is found to be in qualitative agreement with the present determination. Deviations on mean distance and variance values found in previous works could be due to inaccurate modelling of the structural signal and to the effect of the double-electron excitation channels in the background. However, the sensitivity of the EXAFS spectra to the asymmetry of the distribution is very pronounced. In figure 3(c), we show the result of the best-fit calculated EXAFS that can be obtained using a simple Gaussian first-neighbour distribution (calc no asym). The residual curve contains unexplained structural signal related to the effect of the asymmetry of the distribution (mainly the rise of the first peak). The quality of the fit is unacceptable (R function is about 3 times the expected value) and the final values of distances and variances ($R \simeq 3.25$ Å and $\sigma^2 \simeq 0.025$ Å^2) depart considerably from the correct values, similarly to previous findings [29].

This result shows that the skewness parameter β is measured with relatively high accuracy, as it can be seen in table 3. Its value is in substantial agreement with MD simulations. Therefore, provided that accurate experimental spectra and data-analysis are performed, reliable information on anharmonicity and shape of interatomic potential can be inferred from EXAFS data. The negative result obtained in a previous study [39] has to be reconsidered in light of the new advances in data-analysis procedures [20, 21].

The reconstructed Br–all pair distribution function $g(r)$ of solid KBr at 300 K is shown in figure 5(a). Comparison with MD simulation ($\diamond$) shows that the first peak of the pair distribution is slightly shifted toward shorter distances, the rise of the peak being steeper.

Table 3. Structural parameters related to the first four neighbour shells in solid KBr obtained by EXAFS at room temperature and near the melting point. Average distance R, variance σ^2, skewness β (dimensionless) and coordination number (deg) are specified for each shell. Statistical errors on derived parameters are shown in brackets. Structural values are in good agreement with results of MD simulations contained in table 1. The third cumulant $K_3 = \sigma_1^3 \cdot \beta_1$ of the first-shell distribution is also shown (in brackets) for sake of comparison with previous data. The lower part of the table contains previously published first-shell structural values. The dimensionless β_1 value corresponding to the third cumulant of the distribution is also reported (in brackets).

Shell (deg)	Parameters	$T = 300$ K	$T = 940$ K
EXAFS (this work)			
I (6)	R_1 (Å)	3.303(4)	3.600(6)
	σ_1^2 (10^{-3}Å^2)	30(1)	182(8)
	β_1	0.59(6)	1.1(1)
	(K_3 (10^{-3}Å^3))	(3.0)	(85)
II (12)	R_2 (Å)	4.67(1)	4.97(4)
	σ_2^2 (10^{-3}Å^2)	32(6)	170(60)
	β_2		0.8(4)
III (8)	R_3 (Å)	5.76(2)	
	σ_3^2 (10^{-3}Å^2)	40(10)	
IV (6)	R_4 (Å)	6.55(5)	
	σ_4^2 (10^{-3}Å^2)	60(20)	
EXAFS [29]			
I (6)	R_1 (Å)	3.243(15)	
	σ_1^2 (10^{-3}Å^2)	16.0	
	(β_1)	(0.3)	
	K_3 (10^{-3}Å^3)	0.6	

This effect is principally due to the skewness parameter β. The other shells basically agree within the error limits.

EXAFS data analysis has been performed also on solid KBr near the melting point. In figure 6(a), we compare the experimental spectrum with that calculated using the model structure provided by MD simulations. There is only qualitative agreement between the two spectra, as shown by the high value of the R function (about 4 times the expected value) and by the oscillation of the residual curve. The reduction of amplitude of the structural signal with respect to the 300 K spectrum (note the change in the scale) is due to the high level of thermal disorder. The structural signal is dominated by the first-neighbour low-frequency contribution and can be fully explained using the first two $g(r)$ peaks. In figure 6(b), we compare the best-fit calculated EXAFS with experimental data. The agreement is very good and the residual function R is very near to the expected value.

Optimized structural parameters of the first two shells are reported in table 3. As can be observed in figure 5(b), the first-neighbour peak measured by EXAFS is found to be more asymmetric than that calculated by MD. The more interesting effect is that the rise of the first-peak is found to be substantially steeper and the foot is shifted to longer distances. The repulsive part of the interatomic potential used in present MD simulations is found to be too soft in solid KBr. However, while the average first-neighbour distance is about 3.6 Å, the most probable value is still around 3.25 Å, as expected. The shift in the average distance reported in table 3 is mainly due to the skewness of the distribution.
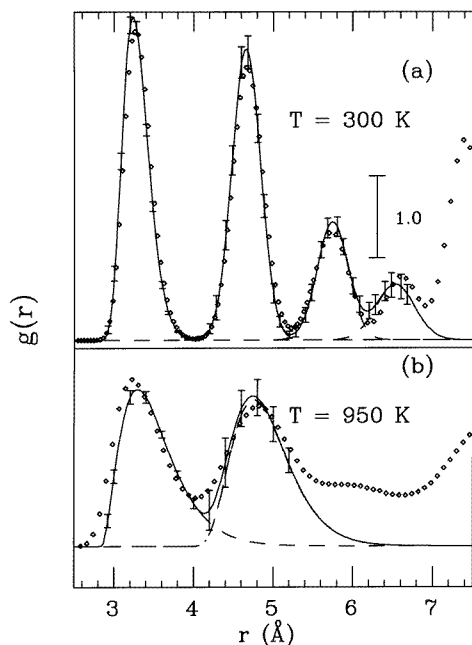
Figure 5. Upper panel (a): total Br–all pair distribution function $g(r)$ of solid KBr at 300 K as determined by EXAFS data-analysis (solid line). Individual shell distributions are shown dashed. Error bars on reconstructed $g(r)$ have been computed starting from statistical errors on individual parameters of table 3. The measured first-shell distribution (first peak) is slightly shifted toward shorter distances; the other shells agree within the error limits with MD simulations ($\diamond$). Lower panel (b): comparison between total Br–all $g(r)$ derived from EXAFS (940 K) and calculated from MD ($\diamond$) at 950 K. The first-neighbour distribution is measured with relatively high accuracy. The foot of the distribution is slightly shifted toward longer distances with respect to the high-temperature MD simulation.

4.2. Liquid KBr

The EXAFS spectrum of liquid KBr at 1025 K, just above the melting point ($T_m = 1007$ K), has been analysed using the starting model provided by MD simulations presented in section 3. The Br K-edge $\chi(k)$ EXAFS signal related to the liquid structure can be calculated starting from the partial distribution functions shown in figure 2(b), using $\gamma^{(2)}$ MS contributions generated using similar procedures as in the solid KBr case [20]:

$$\chi(k) = \int_0^\infty \mathrm{d}r\, 4\pi r^2 \rho_K\, g_{BrK}(r)\, \gamma^{(2)}_{BrK}(r, k) + \int_0^\infty \mathrm{d}r\, 4\pi r^2 \rho_{Br}\, g_{BrBr}(r)\, \gamma^{(2)}_{BrBr}(r, k) + \cdots (4)$$

where $\gamma^{(2)}_{BrK}(r, k)$ and $\gamma^{(2)}_{BrBr}(r, k)$ are the MS two-body signals associated with couple of atoms at distance r while ρ_{Br} and ρ_K are the partial atomic densities of the two chemical species (equal in the present case). Three-body contributions are neglected in (4). This approximation is justified in the present case due to the intrinsic low intensity of the three-body signals found in the high-temperature spectra of solid KBr and to the absence of covalent bonding.

In crystalline systems the pair distribution functions can be easily decomposed in a sum of well-defined peaks, but in liquids those functions present very broad features. Examples of calculation of the EXAFS signal in highly disordered systems like monatomic liquids
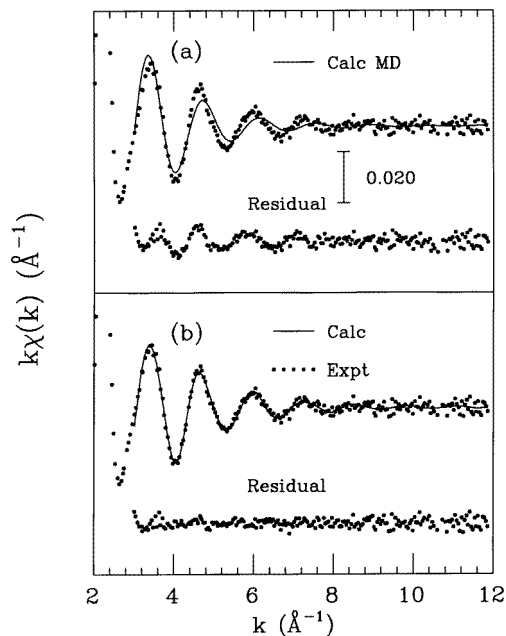
Figure 6. Upper panel (a): Br K-edge experimental EXAFS signal (dots) of solid KBr near the melting point ($T = 940$ K) compared with the calculated signal obtained using the model structure provided by MD simulations (Calc MD). There is no quantitative agreement between the two spectra, as shown by the residual curve. Lower panel (b): comparison between the experimental (dots) and best-fit calculated (Calc) signals. Calculated signal is dominated by the first-neighbour low-frequency contribution.

and amorphous materials can be found in [22–26]. As a matter of fact, EXAFS $\chi(k)$ signal is sensitive only to short-range features and the dominant contribution is usually associated with the first peak of the $g(r)$. Three-body and second-neighbour signals can usually be detected in the presence of covalent or nearly covalent bonds [22, 23, 26].

The EXAFS signal is extremely sensitive to the short-range structure, due to the local nature of the $\gamma^{(2)}$ functions, and a reliable refinement of the first peak of the $g(r)$ can be then attempted. A convenient decomposition of the partial distribution functions is shown in figure 2(b), where the dashed curves are short-range peaks ($g_{BrK}^{(S)}$ and $g_{BrBr}^{(S)}$) and the dot-dashed curves are the long-range oscillatory tails. In figure 7, we compare the experimental EXAFS $k\chi(k)$ structural signal of liquid KBr at 1025 K with that calculated using the model structure provided by MD simulations.

The decomposition of the calculated signal is as follows:

$$
\begin{aligned}
\chi(k) = {} & 4\pi\rho_K \int_0^\infty \mathrm{d}r\, r^2\, \gamma_{BrK}^{(2)}(r,k) \left[g_{BrK}^{(S)}(I)(r) + g_{BrK}^{(S)}(II)(r) + g_{BrK}^{(tail)}(r) \right] \\
& + 4\pi\rho_{Br} \int_0^\infty \mathrm{d}r\, r^2\, \gamma_{BrBr}^{(2)}(r,k) \left[g_{BrBr}^{(S)}(r) + g_{BrBr}^{(tail)}(r) \right] \\
= {} & \gamma_{(S)\,BrK(I)}^{(2)}(k) + \gamma_{(S)\,BrK(II)}^{(2)}(k) + \gamma_{(tail)\,BrK}^{(2)}(k) \\
& + \gamma_{(S)\,BrBr}^{(2)}(k) + \gamma_{(tail)\,BrBr}^{(2)}(k) .
\end{aligned}
\tag{5}
$$
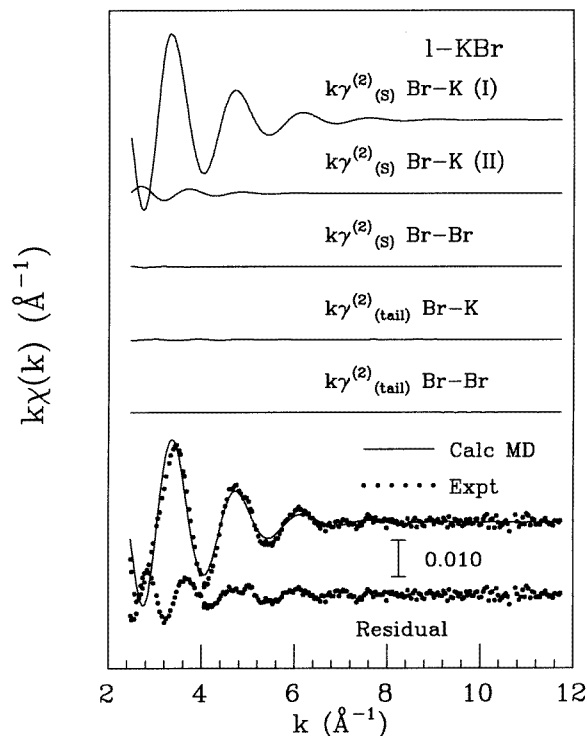
Figure 7. Experimental EXAFS $k\chi(k)$ structural signal (dots) of liquid KBr at 1025 K compared with multiple-scattering (MS) two-body signals (solid lines) calculated using the model structure provided by MD simulations. The various $k\gamma^{(2)}$ signal correspond to the decomposition of the partial pair distribution functions. The dominant signal is associated with the first-neighbour K atoms as shown by the two $k\gamma_S^{(2)}$ Br–K (I) and (II) signals (upper curves). The other curves, accounting for the the Br–Br distribution functions and for the tail of the Br–K one, show a very low intensity. There is a qualitative agreement between the sum of the multiple-scattering signals (Calc MD) and the experimental spectrum (Exp, dots). A residual oscillation at higher frequency is found (bottom curve), especially in the low k-range.

The $\gamma^{(2)}$ signals obtained using the decomposition of the partial distribution functions, appearing in the rhs of (5), are shown in figure 7 (upper curves). The dominant contribution is associated with the first-neighbour distribution ($\gamma_S^{(2)}$ Br–K (I) and (II) signals). The other signals show a very low amplitude. A qualitative agreement between the experimental and the calculated total $k\chi(k)$ signal is found. However, the residual function is about 4 times the expected value and the refinement of the local structure is needed to explain the oscillation found in the residual spectrum, especially at low k values (bottom curve in figure 7).

Using the decomposition of (5), it is possible to refine the short-range part $g^{(S)}(r)$ of the radial distribution [24–26] using Γ peaks and model long-range tails provided by MD simulations. Physical constraints on the $g(r)$ shape, related to the correct thermodynamic limit ($k \to 0$ in the structure factor) can be used allowing a reduction on the number of floating parameters associated with the short-range peaks and consistency with thermodynamic properties (density, compressibility).

In particular, constraints on the structural parameters illustrated in [24] are valid also for the two-component charged liquid under consideration, because the $k \to 0$ limit of the partial structure factors is still $\rho k_B T K_T$ [3]. In the case of the short-range $g_{BrK}^{(S)}(r)$, described by two Γ functions, the constraints are $\Delta(N_I + N_{II}) = 0$ and $\Delta \left[N_I (R_I^2 + \sigma_I^2) + N_{II}(R_{II}^2 + \sigma_{II}^2) \right] = 0$. The coordination number of the short-range $g_{BrBr}^{(S)}(r)$, described by a single Γ function, is also kept fixed. The total number of floating parameters associated with both short-range distribution functions is nine.
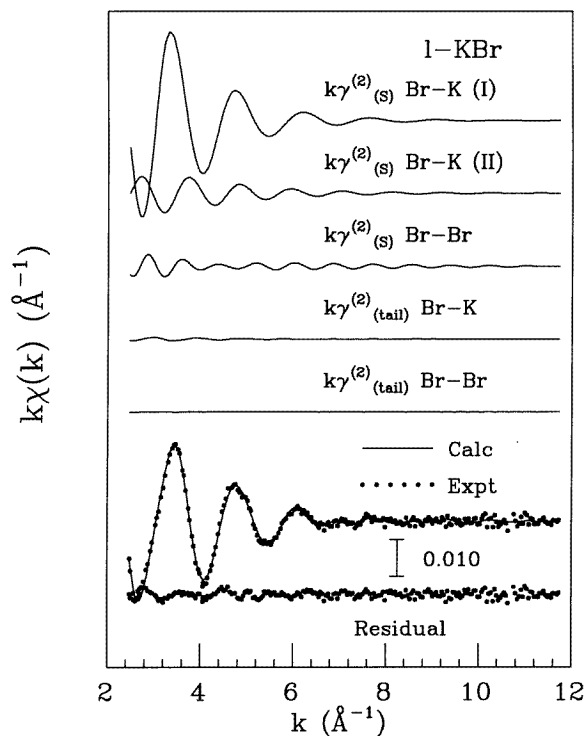

Figure 8. Best-fit calculated $k\chi(k)$ structural signal (Calc) compared with experimental data (dots) of liquid KBr at 1025 K. The agreement is very good, as shown by the residual curve (bottom). The various $k\gamma^{(2)}$ contributions are shown in the upper part of the figure (solid lines).

The final best-fit calculated $k\chi(k)$ structural signal (calc) is compared with experimental data (dots) of liquid KBr in figure 8. The agreement is very good, the residual function almost coincides with the expected value and the residual curve is practically flat. The decomposition of the calculated signal (upper part of figure 8) shows that an increase of the amplitude of the $\gamma_{(S)}^{(2)}$ Br–K (II) and $\gamma_{(S)}^{(2)}$ Br–Br is necessary to get quantitative agreement with experimental data. The presence of these signals allows to explain the oscillatory pattern at low k values found in the residual of figure 7 and even the tiny features in the 6–8 Å^{-1} region. Refined values for the full set of parameters defining the short-range peaks, accounting for the above-mentioned constraints, are reported in table 4. Due to the constraints, many of the parameters are highly correlated (for example N_1 and N_2 are completely anti-correlated) and statistical error bars are intended as maximum (2σ)

Table 4. Structural parameters defining the first peak of the partial $g_{BrK}(r)$ and $g_{BrBr}(r)$ distribution functions in l-KBr as determined by EXAFS data-analysis. Average distance R, variance σ^2, skewness β (dimensionless) and coordination number (deg) are specified for each Γ function (Peak). Only nine independent parameters are actually independent (see text).

Peak	N (deg)	R (Å)	σ^2 (10^{-3}Å^2)	β
g_{BrK}				
I	3.78(8)	3.321(8)	114(8)	0.83(9)
II	1.13(8)	3.92(8)	110(30)	1.1(3)
g_{BrBr}				
I	8.79	5.07(4)	280(160)	1.1(3)
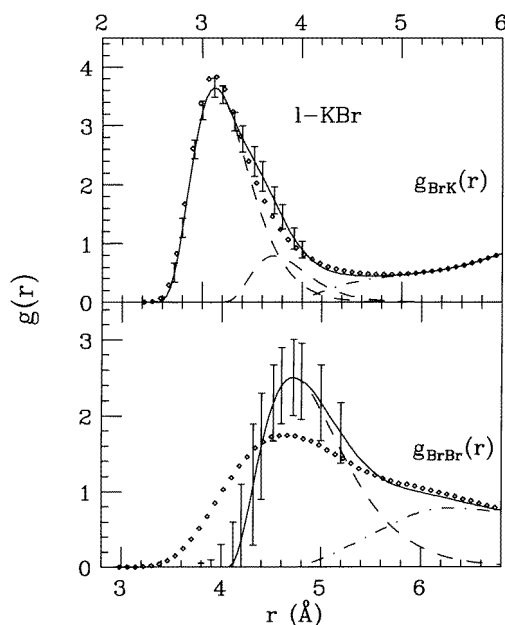
Figure 9. Upper panel: partial pair distribution function $g_{BrK}(r)$ of liquid KBr at 1025 K as determined by EXAFS data-analysis (solid line). Refined Γ functions (dashed) defining the first-neighbour peak and the long-range tail (dot-dashed) are shown. Error bars on reconstructed $g(r)$ have been computed starting from statistical errors on individual parameters of table 4. The shape of the first peak is in substantial agreement with MD simulations ($\diamond$). Lower panel: comparison between partial pair distribution function $g_{BrBr}(r)$ of liquid KBr derived from EXAFS and calculated by MD ($\diamond$). Although affected by large statistical error, the first peak of the Br–Br distribution is found to be more well-defined and shifted to longer distances than that calculated using MD simulations.

uncertainty on each structural parameter.

The reconstructed partial pair distribution functions are shown in figure 9. The shape of the first peak is in substantial agreement with MD simulations ($\diamond$). The first-neighbour peak is found to be slightly more asymmetric than predicted by MD, but position and height are in very good agreement. Comparison with the $g(r)$ distribution of solid KBr at 950 K shows that the maximum of the first peak is shifted of about 0.15 Å toward shorter distances

as already observed in the NaCl case by neutron diffraction [15] In the MD simulations, this effect is reduced. In the lower panel of figure 9 the partial pair distribution function $g_{BrBr}(r)$ of liquid KBr derived from EXAFS and calculated by MD ($\diamond$) are compared. The first peak of the Br–Br distribution is determined with large statistical uncertainty. However, differences with the curve derived using MD simulations are outside of the error bars. The Br–Br peak is found to be narrower and shifted to longer distances. The position of the peak is similar to that found for solid KBr at 950 K. The large penetration obtained in the present MD simulations seems not to be confirmed by experimental data.

5. Conclusions

A detailed study of the local structure of solid and liquid KBr was performed using the x-ray absorption spectroscopy. Accurate sample preparation and data collection techniques allowed us to obtain low-noise Br K-edge EXAFS data for solid KBr near the melting point and liquid KBr. EXAFS spectra were analysed using advanced techniques for data-analysis including multiple-scattering calculations and accounting for double-electron channel contributions in the background. Partial pair distribution functions in liquid and solid KBr derived from EXAFS were compared with molecular dynamics (MD) simulations in similar thermodynamic conditions. EXAFS data were found to be extremely sensitive to the local environment in both solid and liquid phases allowing for accurate refinement of the short-range structure, especially of the first-neighbour Br–K pair distribution. The strong asymmetry of the first-neighbour peak, found in MD simulations even at room temperature, is confirmed by present EXAFS data, which are shown to be very sensitive to anharmonic contributions. MD simulations are found to be in good quantitative agreement with room temperature EXAFS data. The first-neighbour peak at high temperature (near the melting point) derived from EXAFS is found to be slightly shifted toward higher distances and more asymmetric than calculated using MD. In particular, the first rise of the peak is steeper, suggesting a stronger repulsive contribution in the interatomic potential. Short-range g_{KBr} and g_{BrBr} partial distribution functions in liquid KBr were accurately measured for the first time. A good agreement of the first-neighbour g_{KBr} distribution with MD simulations is found, confirming the quality of the present theoretical models. A slight contraction of the most probable first-neighbour distance with respect to high-temperature solid KBr is found. Although measured with less accuracy, the first peak of the g_{BrBr} distribution is found to be sharper and slightly shifted to longer distances, with less penetration inside the first-neighbour K shell than found using MD simulations.

Present results show that accurate and reliable structural information can be obtained using EXAFS spectroscopy in high-temperature solid and liquid systems. Pair distribution functions obtained using computer simulations can be directly compared with experimental data. Application to this simple ionic system (KBr) shows the reliability of present simulation methods. EXAFS spectroscopy can be particularly useful in binary liquids, allowing determination of the short-range part of partial distribution functions and complementing other techniques like neutron diffraction. KBr is one of those cases for which neutron diffraction measurements are not available and where EXAFS is shown to be able to give a unique insight into the local structure.

Acknowledgments

References

[1] Rovere M and Tosi M P 1986 *Rep. Prog. Phys.* **49** 1001
[2] Sangster M J L and Dixon M 1976 *Adv. Phys.* **25** 247
[3] March N H and Tosi M P 1991 *Atomic Dynamics in Liquids* (New York: Dover) (originally 1976)
[4] Woodcock L V and Singer K 1971 *Trans. Faraday Soc.* **67** 12
[5] Adams D J and McDonald I R 1974 *J. Phys. C: Solid State Phys.* **7** 2761
[6] Lewis J W E, Singer K and Woodcock L V 1975 *J. Chem. Soc. Faraday Trans.* II **71** 301
[7] Baranyai A, Ruff I and McGreevy R L 1986 *J. Phys. C: Solid State Phys.* **19** 453
[8] Hansen J P and McDonald I R 1975 *Phys. Rev.* A **11** 2111
[9] Jacucci G, McDonald I R and Rahman A 1976 *Phys. Rev.* A **13** 1581
[10] Copley J R D and Rahman A 1976 *Phys. Rev.* A **13** 2276
[11] Dixon M and Sangster M J L 1976 *J. Phys. C: Solid State Phys.* **9** 3381
[12] Dixon M and Sangster M J L 1977 *J. Phys. C: Solid State Phys.* **10** 3015
[13] Lantelme F, Turq P and Schofield P 1977 *J. Chem. Phys.* **67** 3869
[14] Dixon M and Gillan M J 1981 *Phil. Mag.* B **43** 1099
[15] Edwards F G, Enderby J E, Howe R A and Page D I 1982 *J. Phys. C: Solid State Phys.* **8** 3483
    Biggin S and Enderby J E 1982 *J. Phys. C: Solid State Phys.* **15** L305
[16] Mitchell E W J, Poncet P F J and Stewart R J 1976 *Phil. Mag.* **34** 721
[17] Locke J, McGreevy R L, Messoloras S, Mitchell E W J and Stewart R J 1985 *Phil. Mag.* B **51** 301
[18] Konisberger D C and Prins R (eds) 1988 *X-ray Absorption: Principles, Applications, Techniques of EXAFS, SEXAFS and XANES* (New York: Wiley)
[19] Filipponi A and Di Cicco A 1994 *Nucl. Instrum. Methods* B **93** 302
[20] Filipponi A, Di Cicco A, Tyson T A and Natoli C R 1991 *Solid State Commun.* **78** 265
    Filipponi A, Di Cicco A and Natoli C R 1995 *Phys. Rev.* B **52** 15122
[21] Filipponi A and Di Cicco A 1995 *Phys. Rev.* B **52** 15135
[22] Filipponi A, Di Cicco A, Benfatto M and Natoli C R 1990 *Europhys. Lett.* **13** 319
[23] Di Cicco A and Filipponi A 1994 *Europhys. Lett.* **27** 407
[24] Filipponi A 1994 *J. Phys.: Condens. Matter* **6** 8415
[25] Filipponi A and Di Cicco A 1995 *Phys. Rev.* B **51** 12322
[26] Di Cicco A 1996 *Phys. Rev.* B **53** 6164
[27] Martin C J and O'Connor D A 1977 *J. Phys. C: Sol. State Phys.* **10** 3521
[28] Butt N M, Rouse K D, Thomas M W and Willis B T M 1978 *Acta Cryst.* **A34** 840
[29] Freund J, Ingalls R and Crozier E D 1991 *Phys. Rev.* B **43** 9894
[30] Frenkel A I, Stern E A, Qian M and Newville M 1993 *Phys. Rev.* B **48** 12449
[31] Fumi F G and Tosi M P 1964 *J. Phys. Chem. Sol.* **25** 31
[32] Andersen H C 1980 *J. Chem. Phys.* **72** 2384
[33] Hellwege K-H (ed) 1976 *Structure Data of the Elements* Landolt-Börnstein, Group III, vol III/7 (Berlin: Springer)
[34] D'Angelo P, Di Cicco A, Filipponi A and Pavel N V 1993 *Phys. Rev.* A **47** 2055
[35] Burattini E, D'Angelo P, Di Cicco A, Filipponi A and Pavel N V *J. Phys. Chem.* **97** 5486
[36] Li G, Bridges F and Brown G S 1992 *Phys. Rev. Lett.* **68** 1609
[37] Di Cicco A, Berrettoni M, Marassi R, Tossici R and Filipponi A 1994 *Proc. 9th Int. Symp. on Molten Salts* ed C L Hussey, D S Newman, G Mamantov and Y Ito (*Proc. Electrochemical Society*) vol 94-13, p 77
[38] Tyson T A, Hodgson K O, Natoli C R and Benfatto M 1992 *Phys. Rev.* B **46** 5997
[39] Freund J *Phys. Lett.* **157A** 256